T.1: Soft x-ray optical behaviour: a tool to determine compositional details in thin films of compound materials

Mohammed H. Modi

Soft X-ray Applications Lab,
Synchrotron Utilization Section
Email: modimh@rrcat.gov.in

Abstract

In the soft x-ray region, the contrast in optical constants is sufficiently high for thin films of low atomic number elements. Near the absorption edges the energy-dependent atomic scattering factor gives a resonant behaviour and offers an opportunity to enhance the optical index contrast further. Reflectivity beamline is used to measure optical constants and analyze compositional details of various thin films of low atomic number elements. Details of such studies carried out on thin films of silicon based compound materials are discussed in the theme article.

1. Introduction

With the availability of synchrotron radiation sources, the use of soft x-ray /vacuum ultraviolet (VUV) radiation (10 Å $<\lambda<$ 1000 Å) has increased to explore the various physical and chemical properties of the materials. Use of soft x-ray radiation has increased significantly in various branches of pure and applied science like spectroscopy, microscopy, lithography, astronomy etc. [1], [2] and thereby demand of sophisticated optical instrumentations has also increased. However, design of optical devices requires accurate knowledge of optical parameters i.e. the optical constants. A comprehensive tabulation of optical constants is generated by Henke *et al.* [3] where optical constants for materials Z=1 to 92, in energy range of 10 to 30000 eV are compiled. Moreover, their data mostly rely on absorption measurements and theoretical calculations, thereby many times it is found the tabulated data are varying specially near the absorption edges. These data are reliable in the region away from the absorption thresholds. Near the absorption edges or in anomalous dispersion region, refractive index is sensitive to chemical environment, so any change in local environment of the atom will affect the optical parameters also. The poor reliability of available data and the lack of experimentally measured data for most of the materials have attracted the researchers to generate more reliable optical datasets.

In x-ray region, refractive index is defined as $n=1-\delta+i\beta$, where δ (delta) is decrement index and β (beta) is absorption index and these are called optical constants. These parameters are related to atomic scattering factors for photon energy > 50 eV, where, the interaction of photons with an atom is considered rather than with condensed state of the matter. Further, for x-rays the real part of refractive index is less than unity and in general 'δ' is a positive number, although in vicinity of absorption edges it is not strictly true, e.g. near the Si-L edge $\delta<0$, where the coherent scattering factor decreases due to strong dispersion [4]. The sign reversal phenomena in the real part of refractive index can be understood with the knowledge of response of bound and free electrons contribution to the scattered field. The bound electron contributes to the scattered field with in-phase polarization whereas the free electron contributes with out of phase polarization. In the vicinity of absorption edges the electron is not able to move out of the local environment of the atom and thereby contributes to the scattered field with in-phase polarization. However, when the incident photon energy is sufficiently high to bring the electrons out of local environment of the atom and thereby contributes to scattered field with out of phase polarization. When the in-phase polarization contribution surpasses the out of phase polarization component the real part of refractive index undergoes sign reversal. This phenomena in general is strong near $L_{2,3}$ edge region.

Since, the atomic scattering factor, which is used to describe the refractive index is a complex quantity, its imaginary part can be derived from absorption measurements. By applying a Kramers-Kronig integral transform method [5] the real part of scattering factor is obtained. This method requires the information of absorption index over a full spectral range to determine the value of δ for a particular wavelength. The tabulation of Henke *et al.*[3] is based on this method. They used interpolation technique to determine the imaginary part of refractive index in the intermittent energy region where the absorption measurements are not performed. Nevertheless, the interpolation method may generate errors in the absorption values and in turn introduces uncertainties in the calculations of other counterpart i.e. δ values. Furthermore, these tabulations are based on independent atom approximation that essentially ignores the chemical effects. But at low energies this approximation is no longer valid as contributions from the valance or conduction band electrons also affect the optical responses. In addition, the local environment of an atom may influence the absorption characteristics near the absorption threshold. So, the approximation of an independent atom model is mostly valid in high-energy regime. It is more appropriate to generate the optical constants using the experimental approach.

Determination of optical constants and refractive index in soft x-ray/ VUV region is very useful as absorption edges of most of the elements lies in this photon energy region, enabling one to perform spectroscopic analysis of complex samples using refractive index measurements. Angle dependent reflectivity technique provides information of optical constants. This method has an advantage over transmission measurements as both δ and β can be deduced simultaneously and measurements are carried out on bulk thin film samples. The drawbacks of this method include its sensitivity to surface contamination and roughness. Grazing incidence x-ray reflectivity (GIXR) using Cu K_α radiation is an non-destructive tool to probe thin film structural parameters such as thickness, surface/ interface roughness and density profile [6]. In conventional GIXR, normally, contrast in the optical constant is not sufficient for thin films of low atomic numbers to identify the small compositional gradients at the interfaces. However, near the absorption edges, energy-dependent atomic scattering factors give resonant behaviour [7] and offer an opportunity to enhance the optical index contrast among the low atomic number films. This can be achieved by tuning the energy of x-rays to the absorption edges of specific elements to be investigated. Resonant soft x-ray reflectivity (R-SXR) has been used for the characterization of organic and low contrast thin films [8]. The technique is used to determine depth resolved spectroscopic information of magnetic thin films and artificial heterostructures [9]. Recently, R-SXR has been used to derive quantitative, spatially resolved orbital occupation depth profiles in $LaNiO_3/LaAlO_3$ superlattices [10]. The technique is demonstrated for atomic-layer-resolved elemental concentration sensitivity [11], and probed polarity-induced electronic reconstruction effects in $LaCoO_3$-based heterostructures [12].

Further, optical index profile derived over extended wavelength region of soft x-ray regime combined with soft x-ray reflectivity (SXR) technique can be used to obtain a depth graded compositional details. This technique of optical index modelling in the soft x-ray region has been used to determine compositional details of various compound materials such as zirconium oxide [13], aluminium oxide [14], silicon rich silicon nitride (SRSN) films [15] etc.

2. Theoretical background

Atoms are comprised of massive nucleus surrounded by various electrons having discrete binding energies. According to semi-classical model, the refractive index of a material can be described by solving equation of motion of electrons undergoing forced and damped harmonic oscillations in vicinity of impinging wave field. Under the influence of incident wave of frequency ω, the electrons oscillate with same frequency. Various electrons bound with different restoring forces, exerted by massive positively charged nucleus, respond differently to the impressed wave field. The forced and damped harmonic oscillations of electrons, driven by the Lorentz force exerted by the incident electric fields ($E=E_o e^{-i\omega t}$) can be written as [16]

$$m\frac{d^2x}{dt^2} + m\Gamma\frac{dx}{dt} + m\omega_o^2 x = -eE \qquad (1)$$

where, first term denotes acceleration, second denotes damping force with Γ as a damping constant, and third term denotes restoring force for an oscillator of resonant frequency ω_o. The harmonic displacement 'x' of electrons, which causes the dipole moment and in turn polarization (P=αE) can be written as

$$x = \frac{eE_o m}{(\omega^2 - \omega_o^2 + i\Gamma\omega)} \qquad (2)$$

If the polarisability is known, the dielectric constant ε can be obtained. The refractive index n, which is square root of ε, is given as

$$n(\omega) = 1 - \frac{N_a r_e \lambda^2}{2\pi}\sum \frac{g_s \omega^2}{\omega^2 - \omega_s^2 + i\Gamma\omega} \qquad (3)$$

where r_e is electron classical radius, N_a is number density of atoms. The term g_s is oscillator strength, which in semi classical model defined as the number of electrons with a resonance frequency ω_s. $n(\omega)$ has a strong frequency dependence which causes a dispersion of waves because of variation in phase velocities.

3. Atomic scattering factor

Atomic scattering factor is defined as the ratio between scattered electric field from an atom relative to the scattered field from a free electron. In x-ray region, photon energies are high compared to binding energies of the electrons, the chemical effects are negligible and the refractive index of a compound is calculated using scattering factors of the individual atoms weighted with density. Further, interaction of radiation with an atom rather than condensed state of material is considered. Total scattering amplitude from a group of atoms is calculated by a vector sum of scattering amplitude from the individual atoms. The scattering factor depends on energy as well as on scattering angle [17]. In case of longer wavelengths and/or small scattering angles an atom is considered as a point scatterer so as to give all scattered waves in phase. Therefore, scattering factor becomes angle

independent. Thus,

$$f(\theta,\omega)=f(\omega) \quad (4)$$

and

$$f(\omega)=f_1(\omega)-if_2(\omega) \quad (5)$$

where real part f_1 is effective number of electrons involved in the scattering and imaginary part f_2 is corresponding to absorption. Since in x-ray region, the frequency of incident wave field ω is much larger than the plasma frequency of material ω_p, the refractive index is close to unity and is defined as [17]

$$n=1-\delta+i\beta=1-\frac{N_a r_e \lambda^2}{2\pi}(f_1-if_2) \quad (6)$$

where

$$\delta \cong \frac{r_e\lambda^2}{2\pi}N_a f_1 \quad (7)$$

$$\beta \cong \frac{r_e\lambda^2}{2\pi}N_a f_2 \quad (8)$$

In high energy or short wavelength region f_1 approaches to number of electrons per atom. Normally, δ and β values lies in the range of 10^{-5}- 10^{-7} for hard x-rays and 10^{-2} – 10^{-3} for soft x-rays. The imaginary part of refractive index is determined from a transmission measurement using the relation

$$T=\frac{I}{I_o}=\exp(-\mu\cdot t) \quad (9)$$

where

$$\mu=\frac{4\pi\beta}{\lambda} \quad (10)$$

where I_o is incident flux, I is transmitted flux through a sample of thickness t for a given wavelength λ. Measurement of T requires an accurate knowledge of film thickness t. The uncertainty in film thickness will affect the accuracy of absorption measurements and in turn the optical parameters. In soft x-ray region, due to high absorption a very thin sample is required for transmission measurement. Fabrication of self-supported ultra thin films is an experimental challenge. The other counterpart δ is calculated from the integral transform of β using a Kramers-Kronig relation

$$f_1(\omega)-Z=-\frac{2}{\pi}\int_0^\infty \frac{\omega' f_2(\omega')}{\omega'^2-\omega^2}d\omega' \quad (11)$$

where Z is atomic number. Equation 11 requires complete knowledge of *absorption* over the broad spectral region to calculate a δ value for a particular wavelength. Any error in the measurement of absorption in one wavelength region may affect the derived values of the other. However, the accuracy of measured experimental data i.e. absorption index, is checked by some integral constraints known as *f sum rule* and can be stated as

$$\int_0^\infty \frac{f_2(\omega')}{\omega'}d\omega'=\frac{\pi}{2}Z \quad (12)$$

These integral constraints arise from the laws of motion and causality principle that describes the temporal response of electrons to applied wave field. The Fourier transform of temporal response described by the laws of motion yields the integral constraints in frequency space. Basically Eq. (12) states that the area under the absorption curve is proportional to number of electrons contributing to absorption. Because of increase in relativistic mass of core electrons in consequence of their speed close to that of light they do not respond to applied field as rapidly as free electrons do. Thus, Z is replaced by an effective Z^* defined as

$$Z^*=Z-\left(\frac{Z}{82.5}\right)^{2.37} \quad (13)$$

This correction is important for higher atomic numbers where electron binding energies become comparable to rest mass of the electron. In high-energy limit f_1 approaches to number of electrons Z in atom, which are contributing to absorption.

The calculation of optical parameters by integral transform method involves difficulties due to limit of absorption/ reflection measurements in the limited frequency spectrum, as the method requires a complete knowledge of f_2 over whole frequency spectrum. However, outside the spectral range of experiments the extrapolations are used but that adds uncertainties in the calculations. Moreover, for absorption experiments, one further needs the extremely thin contamination-free freestanding foils, which is extremely difficult to fabricate.

Angle dependent reflectivity measurements can be used to derive optical constants δ and β simultaneously by the use of Fresnel's reflectivity formulae. For s- and p-polarized reflectivity they are written as

$$R_s=\frac{\left|\sin\theta-\sqrt{\tilde{n}^2-\cos^2\theta}\right|^2}{\left|\sin\theta+\sqrt{\tilde{n}^2-\cos^2\theta}\right|^2} \quad (14)$$

$$R_p=\frac{\left|\tilde{n}^2\sin\theta-\sqrt{\tilde{n}^2-\cos^2\theta}\right|^2}{\left|\tilde{n}^2\sin\theta+\sqrt{\tilde{n}^2-\cos^2\theta}\right|^2} \quad (15)$$

where R_s is *s*-polarized reflectivity for electric field vector perpendicular to plane of incidence, R_p is *p*-polarized reflectivity for electric field vector parallel to plane of

incidence and θ is grazing incidence angle from sample surface. Using these formulae, both parameters δ & β are determined simultaneously from the measured reflectivity data of a given sample. This technique is sensitive to surface roughness and contamination layer. Accuracy of optical constants determined by this technique strongly depends on β/δ ratio [18]. Example of reflectance curve for different β/δ ratio is illustrated in Figure T.1.1. If β/δ ratio is $<<1$ the reflectance curve has a well defined shoulder, and δ can be calculated from critical angle relation

$$\theta_c = \sqrt{2\delta} \quad (16)$$

As β increases or β/δ ratio approaches to unity, the curve become more exponential like. For $\beta/\delta > 1$ critical angle region are not distinguishable and determination of δ and β uniquely is not possible. This is an inherent problem with angle versus reflectivity technique.

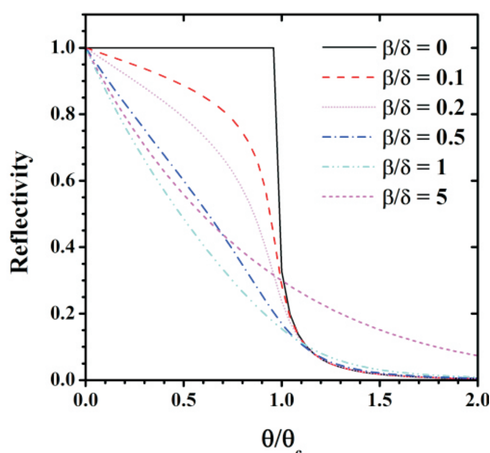

Fig. T.1.1: Effect of β/δ ratio on reflectivity profile calculated for single surface. For $\beta/\delta<<1$ the critical angle region is well defined. As this ratio increases, the curve takes exponential type shape and defining the critical angle position becomes very difficult.

4. The beamlines

To cater the x-ray reflectivity users interested in the soft x-ray energy region, two different beamlines are operational at Indus synchrotron sources. A VUV/ soft x-ray beamline covering energy range of 10-300 eV is operational at Indus-1 synchrotron source [19]. This beamline is useful to probe the K and L absorption edges of low Z elements upto Z=18. To cover other elements like transition metals and rare earth elements another soft x-ray reflectivity beamline with an extended energy region of 100-1500 eV has been designed [20], developed and commissioned at Indus-2 synchrotron source.

4.1 Indus-1 reflectivity beamline (10-300 eV photon range)

The schematic of the optical configuration of the beamline is given in the Figure T.1.2. The beamline is designed to cover 10-300 eV photon energy range (40 – 1000Å wavelength range). The first optical element of the beamline is a vertical deflecting toroidal mirror (TM1) that images the source at 2:1 demagnification on to the entrance slit (S1) of the monochromator. The grazing angle of incidence on this mirror is 4.5º that is sufficiently small to have adequate reflectivity at the lowest photon wavelength of interest. A constant-deviation grazing-incidence toroidal grating monochromator (TGM) is employed in this beamline. The monochromator performs the twin tasks of dispersion and focusing. The TGM covers the desired wavelength range with moderate spectral resolution ($E/\Delta E \approx$ 200-500) and high photon flux (~10^{11} ph/sec) with the use of three toroidal gratings that are interchangeable in-situ without breaking the vacuum. The constant deviation for the monochromator is 162º and the monochromator is used in first positive order. The monochromatic image of the source at the exit slit (S2) is imaged onto the sample position by a vertical deflecting toroidal mirror (TM2) with 1:1 demagnification to get a synchrotron radiation beam spot of ~ 1mm x 1mm. All the optical elements are gold coated and the beamline optical scheme is so chosen that the reflected beam from the post-mirror comes out in horizontal direction.

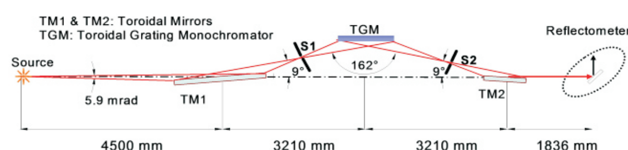

Fig. T.1.2: Optical layout of the Indus-1 reflectivity beamline, which covers photon energy range of 10-300 eV.

The reflectometer at Indus-1 reflectivity beamline consists of a co-axis θ-2θ goniometer. For moving the sample in and out of the beam, a linear translation stage is mounted on the sample rotation stage. The detector distance from the axis of rotation is 200 mm. The goniometer is mounted inside the vacuum chamber and can be set in s- and p- polarization geometry. The vacuum chamber is a cylindrical shell with a diameter of 700 mm. The chamber is pumped by a turbo molecular pump which maintains the high vacuum of ~5×10^{-7} mbar in the chamber while goniometer is in operation. For precise alignment of the reflectometer axes relative to synchrotron beam, the chamber can be aligned in all six degrees of freedom. Silicon photo diodes are mounted on the detector arm to measure the reflected beam. A differential pumping system has been designed and installed to connect the high vacuum reflectometer (1×10^{-6} mbar) with ultra high

vacuum environment of the beamline (~2×10^{-9} mbar).

4.2 Indus-2 reflectivity beamline (100-1500 eV photon range)

The Indus-2 soft x-ray reflectivity beamline uses a constant deviation angle variable line spacing plane grating monochromator (PGM) with Hettrick type optics. This configuration has been chosen because of simplicity of its mechanism and less number of optical elements. The optical layout of the beamline is shown in the Figure T.1.3. This beamline is installed on a 5º port of bending magnet source. The first optical element of the beamline is a horizontally deflecting and vertically mounted toroidal mirror, TM1, which accepts 2 mrad (H) and 3 mrad (V) of the emitted bending magnet radiation. TM1 focuses the light vertically on to the entrance slit S1, and horizontally on to the exit slit S2. The second mirror is a spherical mirror SM, which is vertically deflecting and forms a convergent beam on the plane grating. After SM, the white light is diffracted by the plane grating and desired wavelength is focused on the slit S2. Three interchangeable gratings G1, G2 and G3 of line densities 1200, 400 and 150 lines/mm are used to efficiently cover the whole energy region of 100-1500 eV. The beamline provides moderate spectral resolution (E/ΔE ≈ 1000-6000) and high photon flux (~10^9 - 10^{11} ph/sec) with the use of three gratings that are interchangeable in-situ without breaking the vacuum. The monochromatized light is focused on to the sample by horizontally deflecting and vertically mounted toroidal mirror TM2. The whole beamline operates in ultra high vacuum environment with pressure < 3×10^{-9} mbar.

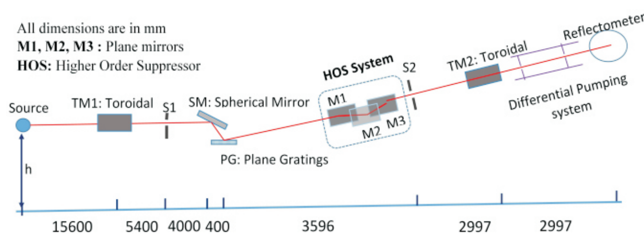

Fig. T.1.3: Optical layout of the Indus-2 reflectivity beamline, which covers photon energy range of 100-1500 eV.

The reflectometer at Indus-2 beamline consists of a two axes high vacuum compatible goniometer with x-y-z sample manipulation stages. The scattering geometry is in the vertical plane which is suitable for s-polarized reflectivity measurements as synchrotron light is plane polarized in the horizontal plane. The sample and the detector are mounted on theta and 2-theta axes respectively. For moving the sample in and out of the beam, a high vacuum compatible linear translation stage is mounted on the sample rotation stage. The sample holder is designed to accommodate big mirror like samples of size up to 300 mm length, 50 mm width and 30 mm height. The maximum weight of the sample in the existing configuration can be about 3 kg. In special case, sample upto 5 kg weight can be mounted. Detector distance from the axis of rotation is 200 mm. The reflectometer has a capability of positioning the sample to within 2 microns and the angular position of the sample can be set within 0.001º. The x-y-z stages can be used as a sample manipulator for undertaking a variety of other experiments. A silicon photodiodes are mounted on the detector rotation axis. Using these detectors, reflectance can be measured over five dynamic ranges. Intensity of the incident beam can be monitored continuously by inserting a Nickel wire mesh in the incident beam and monitoring the photoelectron current from the mesh.

5. Harmonic analysis

Spectral purity of incident beam is very important for reflectivity measurement and subsequent data analysis. Multilayer mirrors are very useful to analyze higher harmonics in the monochromatic radiation coming from a grating monochromator in synchrtron beamlines [21]. Both simulation and analysis of reflectivity data of a multilayer structure can be carried out using different formalisms [6], [22]. Hence, if reflectivity of a multilayer is measured with a beam contaminated with higher harmonics, the available analysis method can be used to determine the fractional contribution of different harmonics if present. Higher harmonics in Indus-1 reflectivity beamline was analysed using a Mo/Si multilayer of d= 97 Å [21]. The similar approach is used to analyse spectral purity of Indus-2 reflectivity beamline using a Ti/Ni multilayer. For harmonic analysis the soft x-ray reflectivity measurements of the Ti/Ni multilayer (45.0 Å Ti/ 45.0 Å Ni)$_{15}$ is carried out in the photon energy range of 1000 eV to 1500 eV. The measured and fitted soft x-ray reflectivity curve is shown in Figure T.1.4. Analysis suggests that the harmonics contamination in this energy region are negligible (< 1%). The detail analysis of measured reflectivity pattern suggest that the multilayer is comprised of four layer periodic structure. There is a 35 Å thick Ti layer, a 38 Å thick Ni layer and two additional interface layers are present i.e. Ti-on-Ni interlayer 8.7 Å thick and Ni-on-Ti interlayer 6.1 Å thick. The roughness of these layers are 5 Å for Ti layer, 8 Å for Ti-on-Ni layer, 8 Å for Ni layer and 5 Å for Ni-on-Ti layer. The same multilayer is used to analyze the harmonic contribution in 100-700 eV photon range also where it is found that the multilayer 'd' value and Ti/Ni contarast is not sufficient for harmonic analysis in the low energy regime, and so that region will be covered by using other suitable multilayer samples.

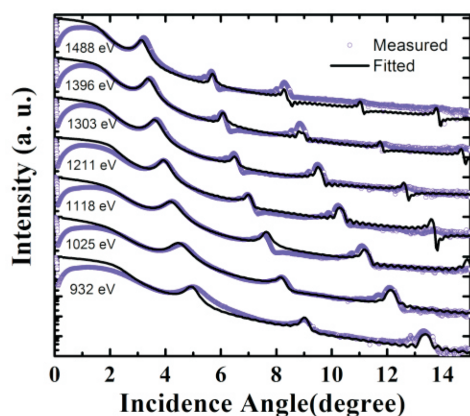

Fig. T.1.4: Soft x-ray reflectivity data of Ti/Ni multilayer measured in 1000-1500 eV photon energy range.

6. Compositional analysis of silicon based thin films

Thin films of low Z elements e.g. C, B, B_4C, Si etc. are very useful for nano meter period multilayer structures and other applications. Analysis of film and interface region in such low Z materials is difficult using hard x-ray reflectivity measurements because of poor optical index contrast between substrate and interfacial layers. In silicon based thin films the values of the energy dependent optical constants change drastically near the Si $L_{2,3}$ absorption edge and thus the SXR technique can be used for compositional analysis by tuning the energy of x-rays near the $L_{2,3}$ edge region. The SXR technique gives the in-depth compositional details of a film in a non-destructive manner [13]-[15], [23].

Structural and compositional details of silicon rich silicon nitride film (SRSN) grown on Si substrate are analysed using the SXR technique [15]. In order to obtain compositional details of the film the SXR measurements are performed near the Si L edge region. The R vs Angle data obtained at different incident wavelengths are analysed to determine the optical constants profile.

A three layer model comprising of (1) the top layer, (2) the principal SRSN layer, and (3) interfacial layer (IL) between SRSN/Si was considered for the structure of the film across its depth. The optical constants δ (dispersion) and β (absorption) are varied to obtain a best fit of SXR data while keeping the all other fitting parameters (thickness and roughness) constant, as those were separately determined from the GIXR analysis. Optical index profile (δ profile) as a function of wavelength near Si $L_{2,3}$ absorption edge as obtained from the SXR fits are shown in Figure T.1.5. From the figure it is evident that the optical index profile of SRSN principal layer lies in between the reference profile of Si and Si_3N_4 obtained from the CXRO website [24]. This indicates that the film is a mixture of Si and Si_3N_4. The presence of Si will induce structural changes and so the values of optical index for SRSN film are shifted from Si_3N_4 towards Si. This simple comparison confirms that the film is Si-rich. This was confirmed with XPS measurements carried out separately [15].

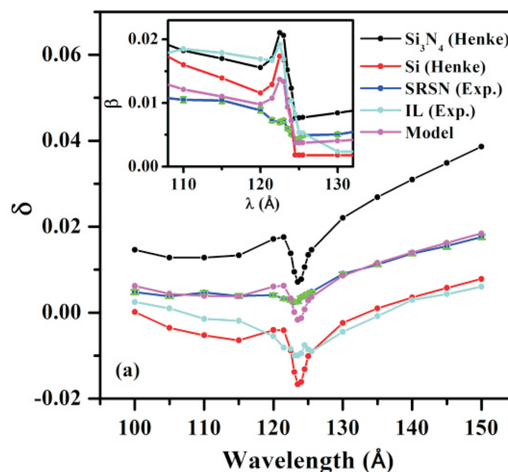

Fig. T.1.5: Measured optical index profile (δ,β) of SRSN film near the Si $L_{2,3}$ absorption edge region is shown alongwith reference profile of Si, Si_3N_4 as obtained from the CXRO database.

Further, for quantitative analysis a volume fraction of these two entities (Si and Si_3N_4) is varied to get the best fit for the measured optical index profile. However, taking into account hydrogen incorporation in SRSN film, a third entity of hydrogen plus void is also included to determine the composition of the film by rigorous calculation. Interestingly, a composition of SRSN film as 30% (H + voids) + 42% (Si_3N_4) + 28% (Si) by volume fraction results into a fit, which is in good agreement with the observed experimental data as shown in Figure T.1.5. Analysis of optical index profile gives reasonable values of film composition non-destructively.

Further, in order to get an insight into the growth of SRSN film, δ profiles were calculated across the depth of SRSN film for various photon energies (Figure T.1.6). A careful analysis of the δ profiles reveals a steep interface with asymmetry in the δ near the region of IL (region 1 in the Figure T.1.6). Presence of both porosity ($\delta \approx 0; \beta \approx 0$) and hydrogen incorporation near Si substrate increases the value of optical index profile for 100.00 and 118.09 eV energy at which Si value is negative. This is evident with the appearance of a hump in the 'region 1' for these energies. At 85.52 eV energy Si value is positive so presence of porosity and hydrogen

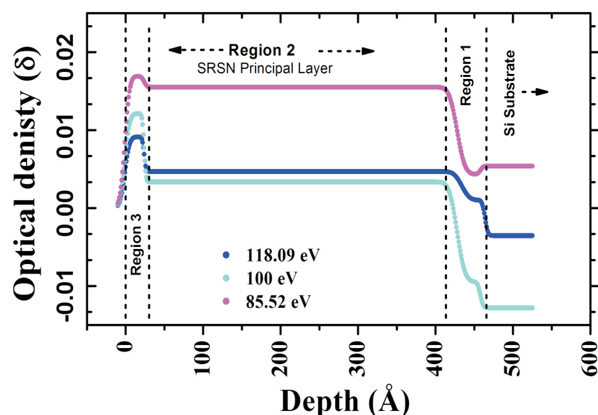

Fig. T.1.6: Optical density profiles across the depth of SRSN film is shown for different photon energies.

decreases the value of optical index profile in comparison to that of Si (see 'region 1' for 85.52 eV energy). The decrease in optical density of the IL corroborates well with the hydrogen incorporated structure. When we move away from the IL, variation in delta appears smooth and near the SRSN/air interface it increases. Increase in optical index profile in 'region 3' clearly indicates reaction of the film with ambient and formation of other Si phases such as SiO_2 and SiO_xN_y at the surface layer. Oxygen incorporation at the surface of SRSN film gives a positive value of δ for all energies. Furthermore, as discussed below, the compositional details obtained from depth profiling data (Figure T.1.6) and optical index profile (Figure T.1.5) together give a clear insight into growth kinetics.

Generally, the SRSN films are deposited with high flux of SiH_4 in comparison to NH_3 by low pressure CVD. In the initial stages of growth SiH_4 molecules are dissociated into higher molecular species SiH_x (x = 0 - 3), either due to electron impact in the discharge or due to thermal dissociation. The higher molecular species so formed are absorbed on the Si substrate surface to form a thin layer of a-Si_x:H with few Si-N atomic bonding, as the sticking coefficient of Si is more. It is due to low mobility of high molecular species, a low density porous Si-rich amorphous hydrogenated silicon nitride (a-$SiN_{x:}$H) interface is formed (mark as 'region 1' in Figure T.1.6). Once the IL is formed the active nitrogen radicals react with this layer to form Si-N-Si bonds and hence the bulk SRSN film (marked as 'region 2' in Figure T.1.6). Finally, when growth terminates the high molecular species comprising Si-H bonds are present at the surface, which in turn react with atmospheric oxygen to form top layer of the silicon dioxide (marked as 'region 3' in Figure T.1.6). The model so presented is consistent with observed results of our SXR measurements and validates the recent atom-by-atom molecular dynamics simulations [25].

The technique is further utilized to distinguish the compositional details of *a*-SiN_x:H films grown in different conditions. These films find diverse applications primarily because they can be deposited over a range of compositions [26], leading to a control over the physical properties. The study of growth kinetics and determination of depth resolved composition can be useful to understand modification of physical properties as a function of composition. Two *a*-SiN_x:H films, named G and R are studied whose compositions were varied by keeping the SiH_4 to NH_3 partial pressure ratios at 0.17 and 0.27 respectively using the PECVD set up (Model: SAMCO PD 2S). The process gases used for film deposition were SiH_4 (4% in Ar) and NH_3. From the UV-Visible transmittance data, the bandgap of 3.7 and 2.7 eV was measured for films G and R respectively. These values lie between the bandgap of *a*-Si_3N_4 [27] and *a*-Si [28], clearly showing that compositions of the two films are different. GIXR analysis of these samples revealed the film is comprised of three layers namely a top oxide layer (OL), expected to be present due to surface oxidation, a middle principal layer (PL) consisting of the deposited sub-stoichiometric *a*-SiN_x:H film and a bottom interfacial layer (IL), which gets deposited before the steady state composition of the middle layer is reached. The thickness and density of G and R films were found to be 112.7 nm, 1.9 g/cm^3 and 133.7 nm, 2.1 g/cm^3, respectively. Densities of samples G and R are significantly (~39%) less than that of bulk Si_3N_4 (3.44 g/cm^3), and attributed to inadvertent presence of hydrogen and sub-stoichiometric compositions of the films.

The SXR measurements of these *a*-SiN_x:H films were carried out by employing x-ray energies close to the Si-$L_{2,3}$ edge. The aforementioned three layer model used to fit the GIXR data for the respective films was used to fit the experimental SXR data. The δ values obtained after fitting the experimental data are plotted in Figure T.1.7 along with the values for c-Si and stoichiometric silicon nitride taken from CXRO website. It is interesting to note that the δ values depicted in Figure T.1.7(R**)** and 7(G), with an exception of the top oxide layer, are quite different for the middle and the interfacial layers of both the films. The δ values of OL (δ_{OL}) are close to SiO_2, indicating that both the films are equally prone to oxidation upon exposure to the ambient. The surface oxidation was also evidenced in XPS Si 2p core level spectra (not shown here) of the films G and R. Further, from Figure T.1.7, it is also evident

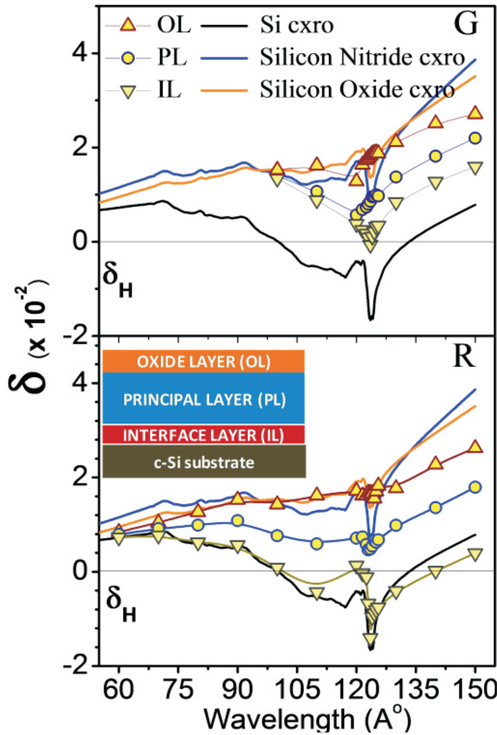

Fig. T.1.7: Optical index profile of three layer region of two a-SiNx:H film (R and G) are plotted alongwith reference profile of Si and Si_3N_4. Schematic of the three layer model assumed for the analysis of the SXR curves is also shown. The δ_H (delta of hydrogen) values are practically zero and are represented by a straight line.

that the IL has a higher Si content as compared to the PL for both films, as in both cases, IL (δ_{IL}) values are reasonably close to theoretical δ values for Si (δ_{Si}). Further, the δ_{PL} of the film R lies closer to δ_{Si} thereby emphasizing its higher Si content. The δ_{PL} for film G are closer to δ_{Si3N4}, showing its proximity to silicon nitride in composition. It shows that the δ values for the films are sensitive to their chemical compositions. As described above and in [15] , by making use of the standard data obtained from the CXRO website, we try to fit the δ_{PL} and δ_{IL} curves for G and R films assuming contributions from volume fractions of Si, silicon nitride and hydrogen and voids. In other words, $\delta_{film} = x.\delta_{Si3N4} + y.\delta_{Si} + z.\delta_H$, where x, y and z correspond to the volume fractions of silicon nitride, Si and hydrogen/voids respectively. The volume fractions so obtained are listed in Table T.1.1. The compositions obtained through this analysis are converted into atomic fractions and compared with the atomic fractions obtained directly from RBS (see [23]). A qualitative agreement between the compositions determined using the two methods adds strength to the presented compositional analysis using SXR. The hydrogen content of the films determined using Elastic Recoil Detection Analysis (ERDA) are found in fair agreement with the results determined from the SXR technique. Further, the respective volume fractions (Si, Si_3N_4 and hydrogenvoids) were multiplied with their densities to obtain the film density. The densities obtained for principal layers of the films G and R are 2.0 and 1.9 g/cm^3 respectively, which are in close agreement with the density obtained from GIXR measurements.

Table T.1.1: Percentage composition of Si_3N_4 phase, elemental Si and H present in the samples G and R as obtained from the fits to SXR experimental data.

Film	Si_3N_4 (3.44) x%	Si (2.33) y%	H + Voids (0.899E-4) z%
G-PL	58	1	41
G-IL	40	20	40
R-PL	45	15	40
R-IL	0	60	40

The depth profiles of optical density (δ-depth profiles) determined from SXR fits are shown in Figure T.1.8. These profiles provide a clear picture of the depth resolved composition of the films. For example, the humps in the OL region (see Figure T.1.8) for both the films G and R are attributed to the presence of SiO_2/SiO_xN_y. The principal layer region in both the films has uniform profile, culminating in the IL region before reaching the substrate. In order to understand the features within the IL region, one must remember that the $\delta_{Hydrogen}$ values are practically zero compared to δ_{Si} and δ_{Si3N4} values (see Figure T.1.7). It may be noted from Figure T.1.7 that $\delta_{Hydrogen}$ is positive with respect to δ_{Si} within a wavelength window of 100-135 Å; therefore the presence of hydrogen is supposed to cause humps in the IL region of the -depth profiles at these wavelengths.

Outside this window, the presence of hydrogen/voids would be indicated by a dips in δ-depth profile. With this understanding, if we look at δ-depth profile, corresponding to 150 Å, of the film R, a dip is observed in the δ values of the IL region, thereby, indicating the presence of hydrogen/voids. However, the δ profiles corresponding to 124 Å and 110 Å do not show a hump as expected, which is because of the comparable thickness (11 Å) and roughness (5 Å) of the IL for sample R. However, the proximity of δ_{IL} values to δ_{Si}, leads us to the conclusion that for the film R the initial growth begins with a thin (11 Å) interfacial layer that approaches c-Si in composition except for the presence of voids/hydrogen which

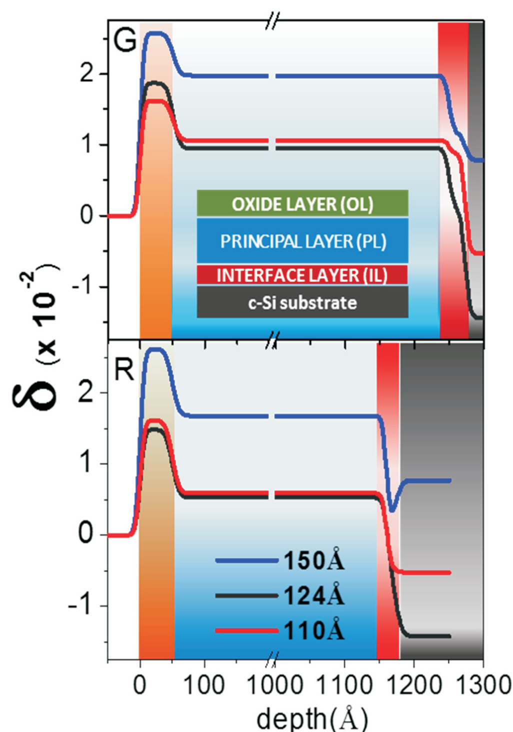

Fig. T.1.8: The optical index profile (δ profiles) across the depth of the films G and R acquired at 150 Å, 124 Å and 110Å incident wavelength are shown.

tend to bring δ values close to zero. Coming to the δ depth profile for the film G, it may be noted that there are humps present in the IL region, thereby indicating that the δ values are positive with respect to the c-Si substrate. Also, the thickness (23 Å) of the IL region in case of film G is higher than that of film R. The humps/positive values can be attributed to the presence of a lower amount of hydrogenvoids as well as to a higher Si_3N_4 component in the IL region of the film G as compared to the IL region of the film R. In general, it can be seen that the IL region, regardless of the sample under consideration, has an invariably higher Si content compared to the principal layer region. This can be understood by looking at the growth mechanism of *a*-SiN_x:H. During the rf-discharge within a PECVD chamber all the precursor gases undergo ionization leading to formation of ionized species of the nitrogen and silicon precursors. Though the gas phase reactions within are complex, broadly two kinds of processes have been identified to be responsible for the deposition of *a*-SiN_x:H. Since the ionized species of the NH_3 have low sticking coefficient compared to those of SiH_4, the initial growth starts with the adsorption of ionized molecular species of SiH_4. However, a simultaneous nitridation of the adsorbed silane related molecular species along with removal of volatile by-products leads to the deposition of *a*-SiN_x:H film [29]. However, the nitridation of adsorbed SiH_x molecular species requires a longer time (due to higher bond-formation/activation energy), and depends on the abundance of the nitrogen precursor (NH_3/N_2). A higher NH_3 flow would, on one hand, increase the possibility of the nitridation of the SiH_x species and on the other hand slow down film growth as the next layer of molecules/atoms has to be deposited on a surface which is composed of both Si and N atoms, unlike the Si surface for initial layer of atoms/molecules. Conversely, increasing the SiH_4 flow would speed up the film growth albeit with the creation of a higher fraction of voids. Thus, one would expect a higher film growth rate for a higher SiH_4/NH_3 flow ratio and vice versa.

It may be noted that the δ values for the film G (Figure T.1.7) near the Si $L_{2,3}$ edge cannot be fitted well using the linear combination of δ values weighted with their volume fractions. This may be due to a possible edge shift of the δ values towards higher energies due to an increase in coordination of Si atoms with Nitrogen atoms going from R to G. It is interesting to note that similar magnitude of edge shift (3.3eV) was observed in the Si-$L_{2,3}$ absorption edges in x-ray transmission measurements on silicon nitride membranes by Delmotte *et al.*[30].

In summary, optical index profile derived over extended energy region of soft x-ray regime using SXR technique has been utilized to obtain depth graded compositional details and growth kinetics in silicon based thin films. We have demonstrated this approach near the Si $L_{2,3}$ edge for non-destructive characterization of SRSN and, a-SiNx:H films.

The author would like to thank Dr. T. Ganguli for his support and encouragement. Thanks are due to Drs. Pankaj Srivastava, S. Singh, Ravi Bommali, Amol Singh, Miss Mangalika Sinha, R.K. Gupta, P. Yadav, Udit Dewangan for their help and contributions at various stages during the course of different studies performed at the reflectivity beamlines.

References

[1] J.H. Underwood, T.W. Barbee, Nature 294, 429 (1981).

[2] J.H. Underwood, T.W. Barbee, D.C. Keith, Proc. SPIE 184, 123 (1979).

[3] B.L. Henke, E.M. Gullikson, and J.C. Davis, At. Data Nucl. Data Tables 54, 181 (1993).

[4] D.Y. Smith, J.H. Barkyoumb, Phy. Rev. B 41, 11529 (1990).

[5] M. Born, and E. Wolf, Principles of Optics, 6th ed. (Pergamon, Oxford, 1980).

[6] L. G. Parratt, Phys. Rev. 95, 359 (1954).

[7] Resonant Anomalous X-ray Scattering: Theory and Application, edited by G. Materlik, C. J. Sparks, and K. Fischer (North-Holland, Amsterdam,1994).

[8] Cheng Wang, T. Araki, and H. Ade, Appl. Phys. Lett. 87, 214109 (2005).

[9] M. Zwiebler, J.E. Hamann-Borrero, M.Vafaee, P. Komissinskiy *et al.*, New J. Phys. 17, 083046 (2015).

[10] E. Benckiser, M. W. Haverkort, S. Brück, E. Goering, S. Macke, A. Fraňó, X. Yang, O. K. Andersen, G. Cristiani, H. U. Habermeier, A. V. Boris, I. Zegkinoglou, P. Wochner, H. J. Kim, V. Hinkov, B. Keimer. Nature Materials 10, 189- 193 (2011).

[11] S. Macke, A. Radi, J. E. Hamann-Borrero, A. Verna, M. Bluschke *et al*., Advanced Materials 26, 6554 (2014).

[12] J. E. Hamann-Borrero, S. Macke, W. S. Choi, R. Sutarto, *et al*. Quantum Materials 1, 16013 (2016).

[13] A. Singh, M. Sinha, R.K. Gupta, M.H. Modi, Appl. Surf. Sci., 419, 337-341 (2017).

[14] M. Sinha, M.H. Modi, Appl. Surf. Sci., 419, 311-318 (2017).

[15] S.P. Singh, M.H. Modi, P. Srivastava, Appl. Phys. Lett. 97, 151906 (2010).

[16] D. Attwood, Soft x-rays and extreme ultra violet radiation: principles and applications (Cambridge University Press, Cambridge, 1999).

[17] E. Spiller, Soft x-ray optics (SPIE, Bellingham, WA, USA, 1994).

[18] R. Soufli, and E.M. Gullikson, Applied Optics 36, 5499 (1997).

[19] R.V. Nandedkar, K.J.S. Sawhney, G.S. Lodha, A. Verma, V. Raghuvanshi, A.K. Sinha, M.H. Modi and M. Nayak, Curr. Sci. 82, 298 (2002).

[20] T. T. Prasad, M. H. Modi, and G. S. Lodha, AIP Proceeding 1234, 369 (2010).

[21] Mohammed H. Modi, R.K. Gupta, Amol Singh, G.S. Lodha, Appl. Opt. 51, 3552–3557 (2012).

[22] S. Banerjee, S. Ferrari, D. Chateigner, A. Gibaud, Thin Solid Films 450, 23-28 (2004).

[23] R.K. Bommali, M.H. Modi, S. Zhou, S. Ghosh, and P. Srivastava, Appl. Surf. Sci. 305, 173-178 (2014).

[24] http://www-cxro.lbl.gov/optical constants/

[25] J. Houska, J. E. Klemberg-Sapieha, and L. Martinu, J. Appl. Phys. 107, 083501 (2010)

[26] Y. Ren, K.J. Weber, N.M. Nursam, Appl. Phys. Lett. 98, 122909 (2011).

[27] A. Rodriguez, J. Arenas, J. C. Alonso, J. Lumin. 132, 2385 (2012).

[28] K. Fukutani, M. Kanbe, W. Futako, B. Kaplan, T. Kamiya, C. M. Fortmann, I. Shimizu, J. Non-cryst. Solids. 227, 63 (1998).

[29] W. A. P. Claassen, W. G. J. N. Valkenburg, M. F. C. Willemsen, W. M.V. D. Wijgert, J. Electrochem. Soc. 132, 93 (1985).

[30] M.F. Delmotte Ravet, F. Bridou, F. Varnière, P. Zeitoun, S. Hubert, L. Vanbostal, G. Soullie, Appl. Optics.41, 5905 (2002).